Nano Energy 46 (2018) 277–289

Contents lists available at ScienceDirect

Nano Energy

journal homepage: www.elsevier.com/locate/nanoen

Full paper

Controlling electric double-layer capacitance and pseudocapacitance in heteroatom-doped carbons derived from hypercrosslinked microporous polymers

Jet-Sing M. Lee[a,*], Michael E. Briggs[a], Chi-Chang Hu[b], Andrew I. Cooper[a,*]

[a] Department of Chemistry and Materials Innovation Factory, University of Liverpool, Crown Street, Liverpool L69 7ZD, UK
[b] Department of Chemical Engineering, National Tsing Hua University, Hsin-Chu 30013, Taiwan

ARTICLE INFO

Keywords:
Porous carbon
Supercapacitor
Hypercrosslinked polymer
Carbonization
Energy storage
N-doped

ABSTRACT

Hypercrosslinked polymers (HCPs) are an important class of porous materials that can be synthesized from aromatic precursors using a one-step "knitting" procedure. This scalable process allows wide synthetic diversity and ease of functionalization. However, pristine HCPs lack electrical conductivity, which limits their potential for electrochemical applications. Supercapacitors are energy storage devices with advantages over conventional batteries such as high power densities, rapid charge speeds, and superior cyclability. In this work, carbonization of functionalized HCPs yields highly conductive and porous materials that can be used as supercapacitor electrodes. Both electric double-layer capacitance (EDLC) and pseudocapacitance (PC) mechanisms are observed. The relative EDLC and PC contributions were quantified for a range of 20 HCP-derived materials, thus allowing a controlled approach to tuning the energy storage properties. The HCP-based carbons show ideal supercapacitor behavior and the best performing material, which shows 63% PC, displays exceptionally high capacitances of up to 374 F g^{-1}, excellent capacitance retention at fast charging speeds, and stability for up to 15,000 charge/discharge cycles.

1. Introduction

As society moves away from fossil fuels, there is a need for higher energy storage capacities and higher power densities in energy storage devices such as batteries [1–3] and supercapacitors [4]. Supercapacitors, also known as electrochemical capacitors, are characterized by high power densities, rapid charge/discharge speeds, and exceptional cycle lifetimes [5]. Supercapacitors store energy either by ion absorption (electric double-layer capacitance, EDLC) or by fast surface redox reactions (pseudocapacitance, PC). EDLC operates by the electrostatic accumulation of charge from the reversible adsorption/desorption of ions and arrangement of polar solvent molecules between the electrolyte and the electrode surface. Thus, the amount of charge stored is proportional to the capacitance of the electrode [6], and hence high surface area materials are advantageous, though a direct linear relationship between capacitance and surface area is not always found [7]. Activated carbon materials are commonly used as EDLC electrodes, with the first patent by Becker awarded in 1957 [8]. There are no Faradic redox reactions in these EDLC electrodes, meaning that the charge storage kinetics are fast and reversible, which allows fast energy uptake and delivery, and hence good power performance. EDLC electrodes are generally very stable because the storage mechanism is purely electrostatic, but this means that EDLC devices also suffer from limited energy densities [7]. Pseudocapacitors operate by fast, reversible, Faradaic redox reactions at the surface of the electrode and they can achieve higher energy densities than the EDLC devices, but this is typically at the expense of power density and cycle life [9]. Transition metal oxides are commonly studied as pseudocapacitor electrodes due to high capacitance contributions from their change in oxidation states. However, because pseudocapacitors can only store charge in the first few nanometres from the surface, this limits these materials being thin films or small particles [7].

Redox-active porous carbons [10–12] can combine the advantages of high power density and cycle life from EDLC with the high energy density from PC. Porous carbon-based supercapacitors have been produced by carbonization of precursors such as biomass [13–15], linear polymers [16–18], graphene oxide [19–21], and a variety of porous organic polymers [10,22,23]. Such routes avoid the use of expensive transition metals, although the performance of organic-based supercapacitors is generally lower [7,24,25]; as such, there is a need for performance improvements in carbon-based supercapacitors. While biomass is a cheap precursor, its limited chemistry, coupled with the

* Corresponding authors.
E-mail addresses: j.lee1@liverpool.ac.uk (J.-S.M. Lee), aicooper@liverpool.ac.uk (A.I. Cooper).

https://doi.org/10.1016/j.nanoen.2018.01.042
Received 3 August 2017; Received in revised form 20 December 2017; Accepted 26 January 2018
Available online 31 January 2018

natural variability between sources of biomass, is a major drawback [26]. Microporous solids have been used as precursors for carbonaceous materials, leading to enhanced properties where the choice of porous precursor affects the functionality of the resultant carbons. Examples of porous precursors include metal-organic frameworks (MOFs) [27–29], porous aromatic frameworks (PAFs) [22,30], and conjugated microporous polymers (CMPs) [10,23,31,32]. Although these materials can show excellent performance as supercapacitor electrodes, these precursor networks involve costly starting materials (*e.g.*, PAFs, CMPs, and many MOFs) and they often require expensive catalysts for their synthesis (*e.g.*, PAFs and CMPs). In addition, some of these precursor networks require preparation under rigorous anhydrous and anaerobic conditions (*e.g.*, PAFs), which further increases the cost of scale-up and reduces potential benefit over transition metal-based supercapacitors.

Hypercrosslinked polymers (HCPs) are microporous materials synthesized from cheap organic monomers using non-rigorous reaction conditions that nonetheless possess potential for synthetic diversification [33]. Permanent porosity in HCPs is a result of extensive crosslinking, which creates a rigid structure that is incapable of complete collapse into a dense, non-porous state upon desolvation. HCPs have been known for many years and are scalable [34,35], with Purolite International Ltd marketing Hypersol-Macronet® polymer resins since the 1990s [36]. HCPs can be prepared from a one-step Friedel-Crafts "knitting" procedure using formaldehyde dimethyl ether as a crosslinker with a very wide range of aromatic molecules, giving access to a large library of functional porous polymers [37]. The surface areas, pore-size distributions, and surface functionalities of HCPs can be tuned by simply changing the aromatic monomer, the reaction stoichiometry, or by the inclusion of functionalized aromatic co-monomers. HCPs have been used extensively in gas storage applications [38–40], separations [41–43], and heterogeneous catalysis [44–46]. However, unmodified HCPs have not been used in electrochemical applications due to their non-conducting nature.

Our aim here was to find a simple procedure to induce electrical conductivity in HCPs, while allowing transfer of heteroatom functionality, and hence to introduce pseudocapacitance into the resulting carbonaceous material. We describe how a simple carbonization process can be applied to a range of HCPs to induce electrical conductivity for use as a supercapacitor electrode. By transferring parent heteroatoms or by applying doping during carbonization, this allowed the HCP-based carbonaceous material to exhibit both EDLC and PC properties, thus yielding high performance supercapacitors.

2. Experimental section

2.1. Materials

Benzene, pyrrole, thiophene, aniline, dimethoxymethane, iron(III) chloride, 1,2-dichloroethane, and poly(vinylidine difluoride) were purchased from Sigma Aldrich. Methanol and *N*-methylpyrrolidinone were purchased from Fisher Scientific. Super C65 carbon black was purchased from Timical. High purity nitrogen was purchased from BOC. All chemicals were used as received without any further purification. Deionised (DI) water was used in purifications.

2.2. Materials synthesis

2.2.1. Synthesis of hypercrosslinked polymers

The hypercrosslinked polymers were synthesized using a previously reported literature method [37]. The monomer (either benzene, pyrrole, thiophene, or aniline; 50 mmol) was added to 1,2-dichloroethane (100 mL) under nitrogen in a 250 mL two-necked Radley's flask equipped with a reflux condenser. Dimethoxymethane (8.8 mL, 100 mmol) was added and the mixture was stirred for 10 min. Iron(III) chloride (16.2 g, 100 mmol) was then added and the mixture was heated at 80 °C overnight. After cooling the dark brown/black precipitate was filtered and washed with methanol. The solids were further purified by Soxhlet extraction with methanol for 1 day then dried under vacuum at 70 °C for 1 day. Gravimetric yields for all polymers were > 90%. Elemental analysis: HCP-Ben, C: 85.50%, H: 5.45%; HCP-Py, C: 58.80%, H: 5.10%, N: 11.02%; HCP-Th, C: 52.79%, H: 3.20%, S: 23.40%; HCP-Ani, C: 60.56%, H: 3.20%, N: 9.86%.

2.2.2. Synthesis of C-HCP-Δ

In a typical procedure, hypercrosslinked polymer (300 mg) was homogeneously dispersed into a ceramic boat and inserted within a tube furnace. The furnace was purged with N_2 (100 mL min^{-1}) at room temperature for 30 min, heated to the specified temperature at a rate of 5 °C min^{-1}, held at the set point for 2 h, and finally cooled naturally to room temperature. The resultant black powder was used as obtained.

2.2.3. Synthesis of N-HCP-Δ

In a typical procedure, hypercrosslinked polymer (800 mg) was homogeneously dispersed into a ceramic boat and inserted within a tube furnace. The furnace was purged with NH_3 (100 mL min^{-1}) at room temperature for 30 min, heated to the specified temperature at a rate of 5 °C min^{-1}, and held at the set point for 2 h. After 2 h, the gas flow was switched to N_2 and the furnace was allowed to cool naturally to room temperature. The resultant black powder was used as obtained.

2.2.4. Synthesis of P-N-HCP-Δ

This follows the general preparation of N-HCP-Δ but C-HCP-800 was used as a precursor.

2.3. Preparation of electrodes

Graphite substrates (10 × 10 × 5 mm, Well Hand Industrial Corp.) were polished using fine sand paper and sonicated with DI water in an ultrasonic bath for 10 min, then with 0.5 M H_2SO_4 for 10 min, and finally with deionised water for 30 min. The substrates were then dried in an oven at 80 °C overnight. The mass of the electrodes were then measured. Active material (8 mg, 80 wt%) was mixed with Super C65 carbon black (1 mg, 10 wt%) and poly(vinylidine difluoride) (PVDF, 1 mg, 10 wt%) in *N*-methylpyrrolidinone (NMP, 1 mL) solvent. The resulting slurry was homogenised by ultrasonication and a total of 1 mg of the active material mass was coated onto an exposed surface of 10 × 10 mm of the substrate by pipette. The substrate was dried at 80 °C overnight in an oven. Mass loading of the substrate was then measured. The samples were weighed on a 5 decimal place balance.

2.4. Electrochemical measurements

The electrochemical responses were investigated using a EC-Lab SP-200 (Bio-Logic Science Instruments SAS, France) in both a two- and three-electrode configurations in a jacketed cell at 25 °C. In the three-electrode configuration, a Ag/AgCl electrode (Argenthal, 3 M KCl, 0.207 V *vs.* standard hydrogen electrode at 25 °C) was used as the reference electrode and a platinum wire was employed as the counter electrode. A Luggin capillary was used to minimize errors due to ohmic potential (*iR*) drop in the electrolyte. Electrolyte solution was degassed for at least 30 min with N_2. 1 M H_2SO_4 was used as the electrolyte solution for evaluating the capacitive performances. The specific capacitance (C_{sv}) from CV was calculated using the following equation: $C_{sv} = (q_a + q_c)/(2ms\Delta V)$, where q_a and q_c represents the anodic and cathodic charge integrated from the positive and negative sweeps of the CV, m is the mass loading of active material, s is the potential scan rate, and ΔV corresponds to the potential window of the CV. The specific capacitance (C_{sc}) from charge-discharge profiles was calculated using the following equation: $C_{sc} = (I \times t)/(V \times m)$, where I is the discharge current, t is discharge time, and V is the discharge voltage. The capacitance from impedance spectroscopy (C_{si}) was calculated using the following equation: $C_{si} = -1/(2\pi f Z'' m)$, where f is frequency, Z'' is the imaginary

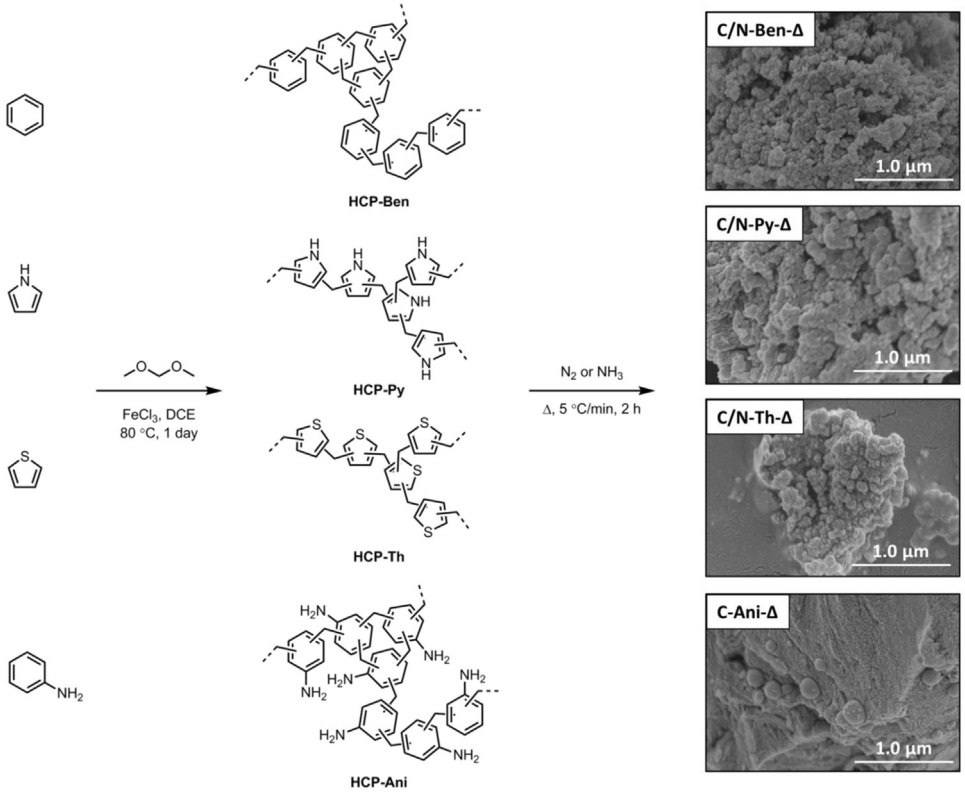

Scheme 1. Synthesis of the hypercrosslinked polymers and subsequent carbonization methods.

part of impedance, and m is the mass of active material. In the two-electrode configuration, graphite-based working electrodes without separator were used in the same jacketed cell. The specific capacitance (C_{sv2}) from CV in the two-electrode configuration was calculated using the following equation: $C_{sv2} = 2(q_a + q_c)/(m_t s \Delta V)$, where m_t is the total mass of active material in both electrodes. The specific capacitance (C_{sc2}) from charge-discharge profiles in the two-electrode configuration was calculated using the following equation: $C_{sc2} = 4(I \times t)/(V \times m_t)$. The capacitance from impedance spectroscopy (C_{si2}) in the two-electrode configuration was calculated using the following equation: $C_{si2} = -2/(\pi f Z'' m_t)$. The energy density was calculated using the following equation: $E = (C \times V^2/2) \times (1000/3600)$. The power density was calculated using the following equation: $P = E/(t/3600)$.

3. Results and discussion

3.1. Methodology of hypercrosslinked polymers and HCP-based carbons

Benzene, pyrrole, thiophene, and aniline were crosslinked according to known literature methods [37]; the resulting polymer networks were referred to as HCP-Ben, HCP-Py, HCP-Th, and HCP-Ani, respectively (Scheme 1). These monomers were chosen to produce a variety of HCPs containing either no heteroatoms (benzene), N-atoms (pyrrole and aniline), or S-atoms (thiophene). Thermogravimetric analysis (TGA) under nitrogen was performed to determine the thermal stability of the HCPs, mimicking the conditions to be used for carbonization (Fig. S1). HCP-Py, HCP-Th, and HCP-Ani all show some mass loss below 100 °C due to the evaporation of physisorbed atmospheric water [39]; this is because the N and S atoms present in these polymers have strong affinities for water. HCP-Ben shows the highest thermal stability, with only 30% mass loss at up to 1000 °C, whereas HCP-Py, HCP-Th, and HCP-Ani show greater mass losses up to this temperature. This is ascribed to the loss of heteroatoms, which are prone to removal during high temperature carbonizations. A good mass recovery was retained after heating the HCPs at high temperatures; hence, these HCPs are suitable candidates for carbonization.

Carbonized HCPs were obtained by direct carbonization under a N_2 atmosphere; the samples were heated at a ramp rate of 5 °C min^{-1} to the set point then held at the set-point for 2 h, before cooling. These carbons are referred to as C-Ben-Δ, C-Py-Δ, C-Th-Δ, and C-Ani-Δ, with Δ signifying the carbonization temperature.

Doping carbons with heteroatoms, such as nitrogen, is known to enhance supercapacitive energy storage due to better dipolar attraction to the electrolyte cations [47], increased electrical conductivity [21], and the introduction of PC contributions [10,48]. C-Py-Δ, C-Th-Δ, and C-Ani-Δ carbons (but not C-Ben-Δ) possess 'native' heteroatoms that are retained from their respective precursors (Table 1). Replacement of the N_2 gas flow with NH_3 for the carbonization process of HCPs allowed the incorporation of additional N groups into the carbons. This process was performed on HCP-Ben, HCP-Py, and HCP-Th, to produce N-doped carbons, which are referred to as N-Ben-Δ, N-Py-Δ, and N-Th-Δ, respectively, with Δ again signifying the carbonization temperature. The post-synthesis treatment of carbons with NH_3 at high temperature also allows the incorporation of nitrogen groups, which has been shown previously to be advantageous for supercapacitive carbon materials [10]. Further studies using C-Ben-800 and C-Py-800 as precursors for the NH_3 post-treatment process produced P-N-Ben-Δ and P-N-Py-Δ, respectively, with Δ signifying the post-treatment temperature.

3.2. Structure and properties of hypercrosslinked polymer-based materials

The apparent Brunauer-Emmett-Teller (BET) surface areas and pore structures of the HCPs and synthesized carbons were investigated by N_2 sorption measurements at 77.3 K (Table 1). The HCPs have surface areas and total pore volumes of 1382 m^2 g^{-1} and 1.52 cm^3 g^{-1} for HCP-Ben, 322 m^2 g^{-1} and 0.25 cm^3 g^{-1} for HCP-Py, 484 m^2 g^{-1} and 0.33 cm^3 g^{-1} for HCP-Th, and 7 m^2 g^{-1} and 0.01 cm^3 g^{-1} for HCP-Ani, respectively. HCP-Ben, HCP-Py, and HCP-Th all exhibit Type II isotherms (Fig. 1), suggesting the presence of macropores within their hierarchical pore structure [49], although it should be stressed that

Table 1
Physical properties of HCPs and carbonized products, and their supercapacitive properties.

Sample	Surface area ($m^2\ g^{-1}$)[b]	Pore volume[a] ($cm^3\ g^{-1}$)		Yield (%)[c]	Elemental analysis (%)				Capacitance ($F\ g^{-1}$)	
		Total pore volume	Micropore volume		C	H	N	S	CV[d]	GCD[e]
HCP-Ben	1382	1.52	0.40	–	85.50	5.45	0.00	0.00	–	–
C-Ben-800	539	0.47	0.21	69	93.40	0.75	0.00	0.00	33	30
C-Ben-900	511	0.42	0.20	64	86.16	0.54	0.00	0.00	34	49
C-Ben-1000	737	0.64	0.28	59	94.32	0.41	0.00	0.00	114	116
N-Ben-600	425	0.36	0.19	71	84.49	1.91	2.16	0.00	100	126
N-Ben-700	458	0.41	0.17	62	83.52	1.20	1.60	0.00	115	130
N-Ben-800	1252	0.96	0.45	40	80.26	1.28	7.50	0.00	267	283
N-Ben-1000	655	0.64	0.24	26	92.43	0.57	1.08	0.00	129	136
P-N-Ben-600[f]	369	0.34	0.16	89	85.15	0.50	1.40	0.00	51	48
P-N-Ben-800[f]	697	0.67	0.28	80	66.50	1.39	5.17	0.00	158	190
HCP-Py	322	0.25	0.14	–	58.80	5.10	11.02	0.00	–	–
C-Py-700	305	0.22	0.14	59	76.35	1.49	9.42	0.00	96	107
C-Py-800	387	0.22	0.16	49	75.20	1.38	8.86	0.00	126	134
C-Py-900	388	0.24	0.15	50	76.85	1.20	6.41	0.00	132	159
C-Py-1000	557	0.35	0.22	39	78.18	1.73	3.24	0.00	108	113
N-Py-600	320	0.23	0.15	54	72.98	2.05	12.73	0.00	58	70
N-Py-700	329	0.47	0.31	53	73.05	1.97	13.44	0.00	284	317
N-Py-800	1484	0.83	0.47	11	72.21	2.13	9.79	0.00	183	237
P-N-Py-600[g]	418	0.29	0.20	95	76.33	1.14	11.52	0.00	135	173
P-N-Py-700[g]	443	0.30	0.21	45	80.45	1.24	8.51	0.00	162	231
HCP-Th	484	0.33	0.22	–	52.79	3.20	0.00	23.40	–	–
C-Th-800	616	0.34	0.25	50	79.32	0.38	0.00	13.58	52	49
N-Th-600	464	0.31	0.21	56	71.80	1.63	7.93	12.38	24	23
N-Th-700	760	0.49	0.34	33	73.95	1.55	13.03	0.94	220	226
N-Th-800	508	0.35	0.22	17	55.50	2.12	7.33	0.00	166	196
HCP-Ani	7	0.01	0.00	–	58.69	5.05	8.54	0.00	–	–
C-Ani-800	376	0.30	0.13	47	88.26	0.35	1.34	0.00	66	66

[a] Calculated by single point pore volume.
[b] Apparent BET surface area.
[c] Carbonization yield by mass.
[d] Specific capacitance measured by cyclic voltammetry at a scan rate of $10\ mV\ s^{-1}$ in 1 M H_2SO_4.
[e] Specific capacitance measured by galvanostatic charge-discharge at a current density of $1\ A\ g^{-1}$ in 1 M H_2SO_4.
[f] Post-synthesis treatment with NH_3 carried out on C-Ben-800.
[g] Post-synthesis treatment with NH_3 carried out on C-Py-800.

these materials can swell in N_2 [50], which might also affect the isotherm shape at higher relative pressures. HCP-Ani exhibits a Type III isotherm due to relatively weak absorbent-absorbate interactions and absorbed N_2 molecules clustering around the most favourable sites on the surface of the non-porous solid. The surface area matches previously reported HCP-Ani [51], which was used for gas separations of CO_2 and N_2 at 300 K.

Nearly all carbonized products display Type I isotherms with a steep uptake at low P/P_0 with Type IVa characteristics, with a hysteresis loop appearing at $P/P_0 = 0.5$, indicative of a hierarchical structure with high levels of micropores and additional mesopores (Fig. S2). In general, carbonizations in a N_2 atmosphere afford carbons with a more microporous structure than the parent polymer, as demonstrated by the narrowing of the micropore-size distributions, a sharper increase in the gas sorption isotherms at low P/P_0, and decreased level of mesopores in the overall pore-size distributions. This was also observed for the low temperature carbonizations in NH_3; however, when high temperatures were used (800–1000 °C) increases in the mesopore content were observed. Carbonizations of HCP-Ben and HCP-Py under N_2 resulted in porous carbons with similar surface areas between 700 and 900 °C (539 and 511 $m^2\ g^{-1}$ for C-Ben-800 and C-Ben-900, respectively, and 305, 387, and 388 $m^2\ g^{-1}$ for C-Py-700, C-Py800, and C-Py-900, respectively, Table 1). However, an increase in surface area was observed at 1000 °C (737 $m^2\ g^{-1}$ for C-Ben-1000 and 557 $m^2\ g^{-1}$ for C-Py-1000). C-Th-800 had a relatively high surface area of 616 $m^2\ g^{-1}$ and C-Ani-800 had a surface area of 376 $m^2\ g^{-1}$. Similarly, carbonizations under an NH_3 atmosphere resulted in broadly equivalent surface areas for HCP-Ben and HCP-Py at 600 and 700 °C, but an increase was observed at a higher temperature of 800 °C. N-Py-800 yielded the highest surface area of 1484 $m^2\ g^{-1}$, closely followed by N-Ben-800 (1252 $m^2\ g^{-1}$), which was due to the additional etching effects from NH_3. Though N-Py-800 yielded the highest surface area carbon from the materials synthesized here, N-Py-700 possessed the highest N-content of 13.44% (9.79% for N-Py-800); both surface area and N-content are important factors for supercapacitor electrodes. Of the carbonized HCP-Th samples, N-Th-700 had the highest surface area of 760 $m^2\ g^{-1}$; unlike N-Ben-800 and N-Py-800, carbonization at 800 °C reduced the surface area to 508 $m^2\ g^{-1}$ due to a decrease in the microporous structure (69% micropore content for N-Th-700 *vs.* 63% for N-Th-800) and probable pore collapse. High temperature carbonization of HCP-Ben at 1000 °C under NH_3 also yielded a lower surface area of 655 $m^2\ g^{-1}$ due to pore collapse (47% micropore content from N-Ben-800 *vs.* 38% from N-Ben-1000). The other HCPs could not be carbonized to 1000 °C due to their lower thermal stabilities, and hence low mass recovery.

Carbonizations of heteroatom-containing HCPs (HCP-Py, HCP-Th, and HCP-Ani) under N_2 resulted in the gradual loss of heteroatom content with increasing carbonization temperature (Table 1). Though C-Ani-800 and C-Py-800 had similar surface areas, C-Ani-800 possessed a lower N-content (1.34%) compared with C-Py-800 (8.86%). This was likely due to the lower initial N-content of HCP-Ani (8.54%) compared with HCP-Py (11.02%) and that the heterocyclic N in HCP-Py may be more thermally stable than the primary aryl amines of HCP-Ani, which allows higher incorporation of N atoms into the carbonized product. For this reason, carbonization of HCP-Ani was not studied further at other temperatures.

We observed an optimal carbonization temperature for incorporating N into the carbonized HCPs under a NH_3 flow. N-Ben-800, formed by the carbonization of HCP-Ben at 800 °C under NH_3, yielded the highest N-content in its series (7.50%) whereas carbonization of HCP-Py and HCP-Th under NH_3 at 700 °C yielded the highest N-content

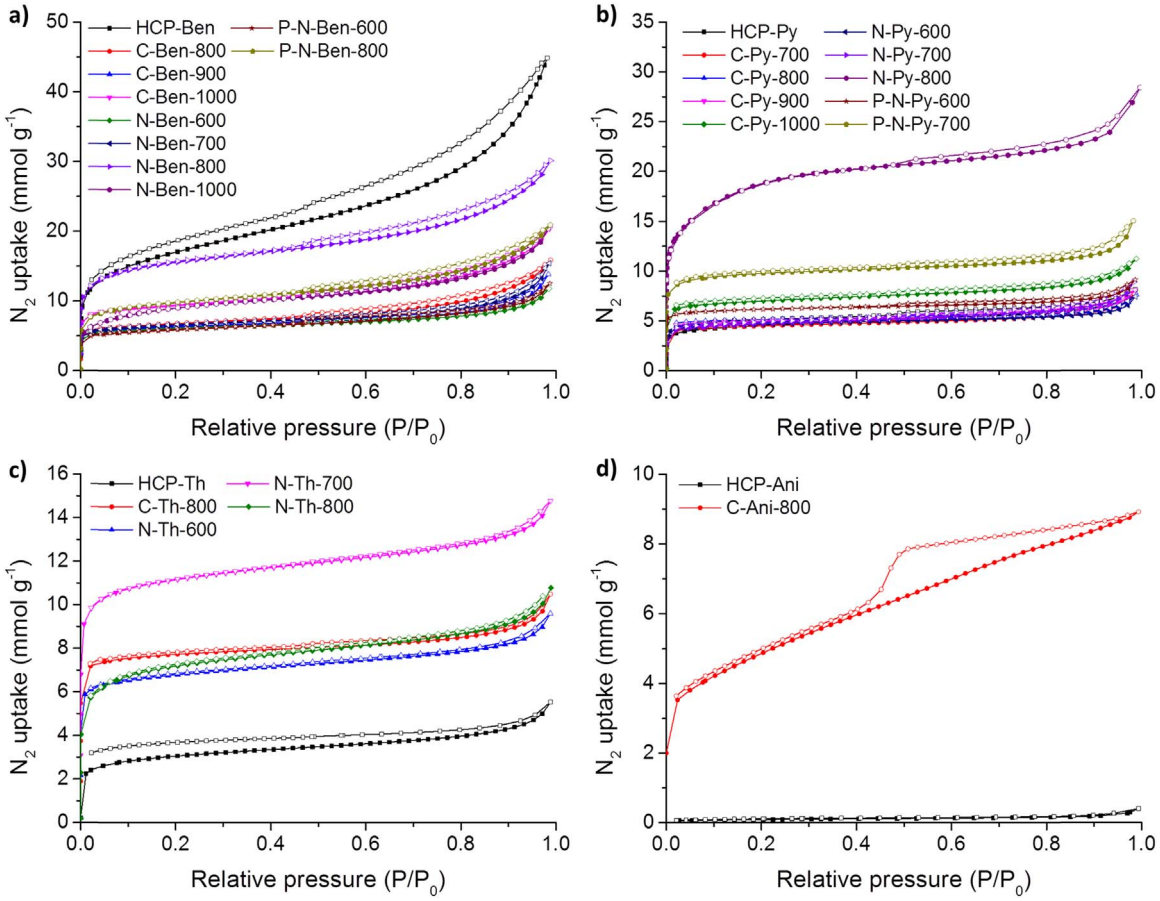

Fig. 1. Nitrogen adsorption–desorption isotherms of (a) HCP-Ben and x-Ben-Δ, (b) HCP-Py and x-Py-Δ, (c) HCP-Th and x-Th-Δ, and (d) HCP-Ani and C-Ani-800 at 77.3 K (the adsorption and desorption branches are labelled with filled and empty symbols, respectively).

(13.44% for N-Py-800% and 13.03% for N-Th-800) in their respective series. During high temperature carbonizations, heteroatoms tend to be more easily removed than carbon [52]; it therefore makes sense that less NH_3 is incorporated into the carbon at very high temperatures. Likewise, if the temperature is too low, carbonization will not fully occur; therefore, intermediate temperatures are required to ensure the formation of a graphitic structure that incorporates the maximum amount of N from NH_3. Interestingly, N-Th-600 contains both high levels of N (7.93%) *and* S (12.38%) atoms. However, when the NH_3 carbonization was increased to 700 °C in the synthesis of N-Th-700, the N content remained high while the S content dropped to 0.94%; further increasing the temperature to 800 °C resulted in total loss of S atoms. It is possible that removal of the S atoms provides space within the structure for integration of additional N as the N-content of N-Th-700 closely matches that of N-Py-700, while N-Th-800 closely matches N-Py-800.

C-Ben-800 and C-Py-800 were N-doped post-synthesized by treatment with NH_3 at various temperatures, which had previously shown positive results with CMP-derived carbons [10]. Post-synthesis doping of C-Ben-800 at 600 °C (P-N-Ben-600) only showed moderate N incorporation of 1.40%. However, using a higher temperature of 800 °C allowed the incorporation of a higher N-content of 5.17% in P-N-Ben-800. The temperature trend is similar for directly carbonized HCPs under NH_3; N-Ben-800 has a much higher N-content than N-Ben-600 (7.50% *vs.* 2.16%). P-N-Py-600 showed a N-content of 11.52%, which was higher than its precursor, C-Py-800, which had a N-content of 8.86%. However, P-N-Py-700 contained 8.51% N, so it can be assumed that no further N-doping occurred at 700 °C. Rather, increase in apparent surface area from 387 to 443 $m^2\ g^{-1}$ is likely due to NH_3 etching further pores within the material, resulting in a 47% mass recovery. Interestingly, although post synthesis N-doping affords carbons with lower N-contents than the direct NH_3 carbonization method—in line with previous studies [10]— the surface area of the P-N-HCP-Δ materials were lower than the N-HCP-Δ series in this study.

Field emission scanning electron microscopy (FE-SEM) was used to study the morphology of the HCPs and the resulting carbons (Fig. S3). The images show similar morphologies for the HCPs and their carbonized products, irrespective of whether they were carbonized under N_2 or NH_3 gas. Therefore, it can be concluded that morphology is well retained when using HCPs as carbonization precursors, which could be advantageous when designing surfaces on HCPs that need to be translated into porous carbons.

Powder X-ray diffraction (PXRD) of the HCPs and carbons are shown in Fig. S4a-d. All HCPs and carbonized products show characteristic peaks at $2\theta \approx 26$ and 44° corresponding to the (002) and (101) planes of hexagonal graphite (JCPDS Card no. 41–1487), respectively [53,54]. The relatively broad peaks suggest that the materials possess a low degree of graphitization and are predominately amorphous [39,55]. Some additional crystalline peaks appeared in various samples that are attributed to small levels of alumina contamination from either the tube used in the furnace or the boat which carried the sample (Fig. S4e). Repeat syntheses were attempted but failed to yield an uncontaminated sample. However, the small levels of alumina did not affect the other characterization methods and supercapacitance analysis.

Raman spectra of the porous carbons show two first-order Raman shifts of carbon present between 1100 and 1800 cm^{-1} (Fig. S5). The disordered (*D*) band at ≈ 1350 cm^{-1} and graphitic (*G*) band at ≈ 1590 cm^{-1} are attributed to the breathing mode of *k*-point phonons of A_{1g} symmetry and the in-plane stretching motion of symmetric sp^2 C-C

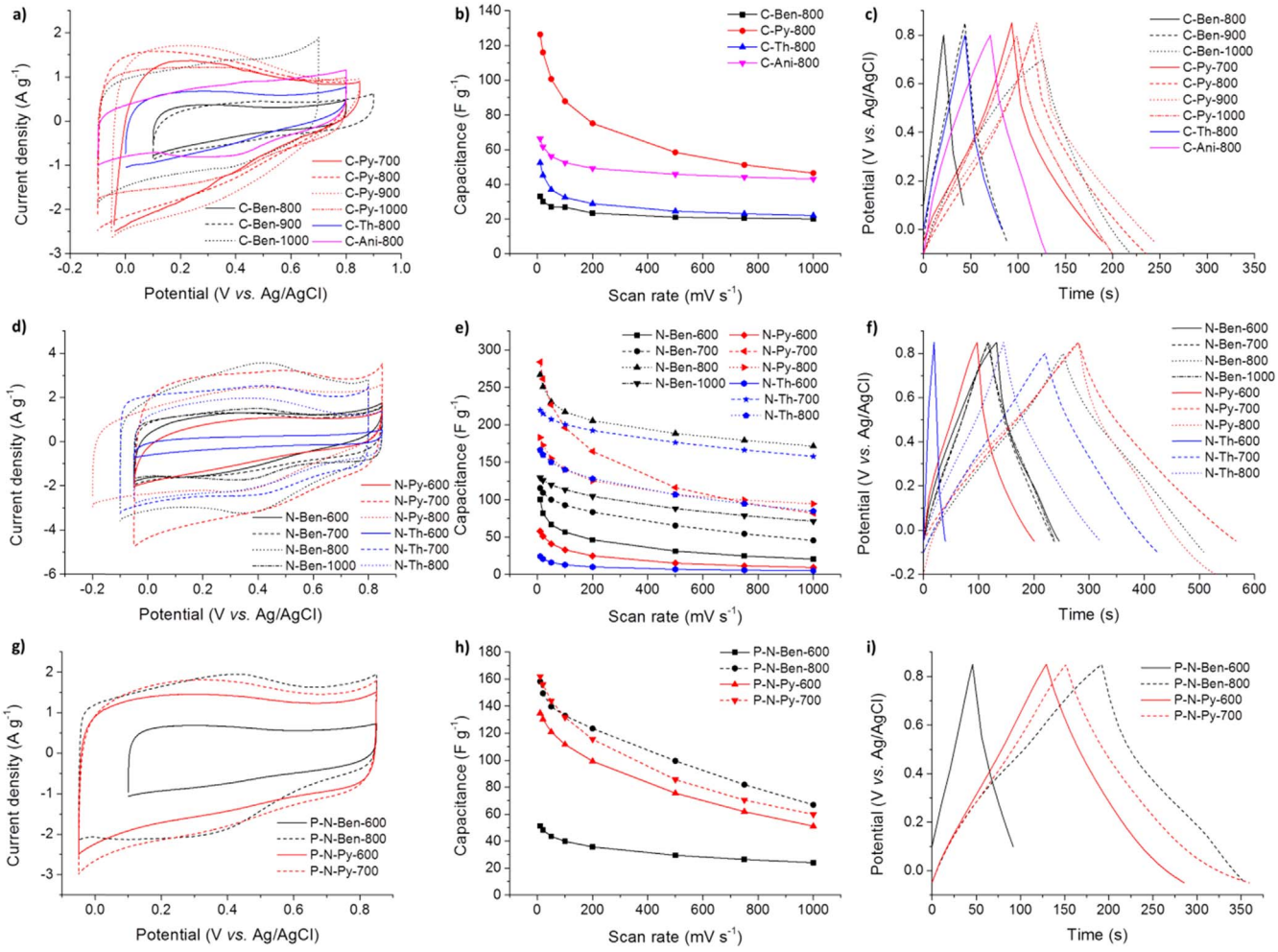

Fig. 2. Electrochemical analysis of all carbonized materials in a three-electrode system in 1 M H_2SO_4. (a) Cyclic voltammograms of C-HCP-Δ at a scan rate of 10 mV s^{-1}. (b) Specific capacitance of C-HCP-800 at varying scan rates. (c) Galvanostatic charge-discharge curves of C-HCP-Δ at a current density of 1 A g^{-1}. (d) Cyclic voltammograms of N-HCP-Δ at a scan rate of 10 mV s^{-1}. (e) Specific capacitance of N-HCP-Δ at varying scan rates. (f) Galvanostatic charge-discharge curves of N-HCP-Δ at a current density of 1 A g^{-1}. (g) Cyclic voltammograms of P-N-HCP-Δ at a scan rate of 10 mV s^{-1}. (h) Specific capacitance of P-N-HCP-Δ at varying scan rates. (i) Galvanostatic charge-discharge curves of P-N-HCP-Δ at a current density of 1 A g^{-1}.

bonds, respectively [10,56]. Carbonizations between 600 and 1000 °C did not lead to a large change between the intensity ratio, I_D/I_G, of the *D* and *G* bands, as it is known that very high temperatures (~2000–3000 °C) are required to form highly ordered graphitic carbon [57]. However, it was noted that the I_D/I_G ratio was largely dependent on the carbonization precursor, with an I_D/I_G ratio for x-Ben-Δ of 2.08–2.49, x-Py-Δ of 2.41–3.01, x-Th-Δ of 2.35–2.80, and C-Ani-800 of 1.78. It was also observed that the I_D/I_G of N-HCP-Δ and P-N-HCP-Δ was generally higher than C-HCP-Δ, likely due to the addition of N atoms increasing defects in the graphitic carbon structure.

3.3. Supercapacitive performances of HCP-based carbons

The electrochemical performances of the HCP-based porous carbons were first evaluated using a three-electrode cell in 1 M H_2SO_4 aqueous electrolyte. The HCPs directly carbonized under N_2, C-HCP-Δ, were initially studied by cyclic voltammetry (CV) at a scan rate of 10 mV s^{-1} (Fig. 2a). The large range of materials tested required various potential windows to be employed to avoid irreversible electrode reactions, such as solvent decomposition and irreversible redox reactions on the electrodes. This avoids over-oxidation and/or over-reduction so that we only record current from the "capacitive potential range" of the material [58]. C-Ben-800, C-Ben-900, and C-Ben-1000 have a specific capacitance of 33, 34, and 114 F g^{-1}, respectively, at a scan rate of 10 mV s^{-1} (Table S1). The increase in capacitance of C-Ben-1000 is likely due to its higher degree of carbonization, observed by the high carbon to hydrogen ratio of C-Ben-1000 (Table 1), and higher graphitic carbon content (Fig. S5). These materials show quasi-rectangular CV curves, which are characteristic of good reversible supercapacitor behavior [59]. As expected, C-Py-Δ, C-Th-800, and C-Py-800 show larger current densities due to the presence of heteroatoms contributing to PC. C-Th-800, which contains 13.58% S, shows a moderate specific capacitance of 52 F g^{-1}, whereas C-Ani-800 exhibits a higher capacitance of 66 F g^{-1} with only 1.34% N. This is likely due to N groups providing larger PC than S groups, which is reflected in the literature by the popularity of N-containing carbonaceous supercapacitors [60–62]. C-Py-700, C-Py-800, C-Py-900, and C-Py-1000 show high capacitances of 101, 126, 134, and 108 F g^{-1}, respectively, due to the high N-content of the carbons transferred from HCP-Py precursor. The increase in capacitance on going from C-Py-700 to C-Py-900 is due to the higher levels of carbonization and resultant graphitization. Though C-Py-1000 had the highest degree of graphitization from its series (I_D/I_G = 2.41), the decrease in capacitance was likely due to lower N-content of 3.24%. Therefore, a balance exists between higher capacitance resulting from higher degrees of carbonization at higher temperatures and a reduction in capacitance due to the concomitant decrease in heteroatom content. When comparing the carbons synthesized at 800 °C from the four HCPs, the precursors are ranked: HCP-Py > HCP-Ani > HCP-Th > HCP-Ben. The capacitance of C-Py-800 rapidly decays at higher scan rates, which is common for PC electrodes; however, it is still higher than the other C-

HCP-800 materials (Fig. 2b). The materials were tested with galvanostatic charge-discharge (GCD) experiments, with the charge-discharge times (Fig. 2c) consistent with the current densities obtained from the CV results. Thus specific capacitances calculated by GCD experiments follow the same trend as for the specific capacitances calculated by CV (Table S2). All the C-HCP-Δ carbons showed a triangular charge-discharge shape, which is typical behavior for constant charge and discharge of supercapacitive materials with good reversibility [10].

The N-doped HCP-based carbons show much larger current responses than the HCPs carbonized under N_2, as observed by CV at a scan rate of 10 mV s^{-1} (Fig. 2d). All N-HCP-Δ samples show quasi-rectangular CV curves. N-Ben-600 and N-Ben-700 have similar specific capacitances of 100 and 115 F g^{-1}, respectively. However, the CV curve for N-Ben-700 exhibits a more symmetrical quasi-rectangular shape denoting higher reversibility, which is likely developed by the harsher carbonization conditions. N-Ben-800 also exhibits a highly symmetrical CV curve but with much larger current responses, yielding the highest capacitance of 267 F g^{-1} from the HCP-Ben precursor. N-Ben-1000 has a decreased capacitance of 129 F g^{-1} due to a lower N-content in the carbon from the high temperature carbonization. However, the higher temperature yields a highly symmetrical and reversible CV curve, which can be compared with N-Ben-600 and N-Ben-700 due to the similar current responses. N-Py-600 has a capacitance of 58 F g^{-1}, while with N-Py-700 the capacitance dramatically increases to 284 F g^{-1}, even though the surface areas and N-content of N-Py-600 (320 m^2 g^{-1} and 12.73%, respectively) and N-Py-700 (329 m^2 g^{-1} and 13.44%, respectively) are similar. A Nyquist plot in the low frequency region shows the impedance of the imaginary part approaches vertical with N-Py-700, indicative of typical ideal capacitive behavior (Fig. S6) [63], whereas the low frequency capacitive behavior of N-Py-600 is shifted along the real axis towards more resistive values [63]. Therefore, the low capacitance of N-Py-600 was ascribed to the low electric conductivity of this material when carbonized at the relatively low temperature of 600 °C. N-Py-800 has a lower capacitance of 183 F g^{-1} due to a decrease in N-content to 9.79%, despite possessing a very high surface area (1484 m^2 g^{-1}). Higher levels of porosity can aid electrolyte ion diffusion and afford higher levels of EDLC. These benefits can be seen with the capacitance retention of N-Py-800 at higher scan rates (Fig. 3e) with 51% capacitance retention at extremely high scan rates of 1000 mV s^{-1}, whereas N-Py-700 only retains 29% capacitance at this rapid scan rate (Table S1). The weak capacitance retention of N-Py-700 is due to the electrode being largely PC-based rather than EDLC-based, which is known to have slower kinetics and lower power density [9]. Interestingly, even though N-Py-800 has a higher surface area and N-content than N-Ben-800, the capacitance is lower. We suggest that the greater hierarchical structure of N-Ben-800 (47% microporous) supports more efficient electrolyte diffusion than N-Py-800 (57% microporous), as it is known that micropores alone are not favourable for quick electrolyte ion diffusion and result in low capacitances [64]. The quicker electrolyte ion diffusion of N-Ben-800 allows higher capacitance retention at 1000 mV s^{-1} of 64%. N-Th-600 has a low capacitance of 24 F g^{-1} due to the same reason as N-Py-600 of low electric conductivity, combined with a lower N-content 7.93%. The 12.38% S in this material was thought to not play a large role, as previously discussed with C-Th-800. N-Th-700 showed a much higher capacitance of 220 F g^{-1} due to its higher conductivity, higher N-content of 13.03%, and a higher surface area of 760 m^2 g^{-1}. Its CV shape is highly symmetrical with a sharp quasi-rectangular shape, which is reflected by its high capacitance retention at 1000 mV s^{-1} of 72%. The combination of a lower N-content (7.33%) and surface area (508 m^2 g^{-1}) for N-Th-800 resulted in a lower capacitance of 166 F g^{-1}. The GCD curves reflect the same trend in capacitive results from CV (Fig. 2f). All N-HCP-Δ materials show typical supercapacitor behavior displayed by the triangular charge-discharge profiles. N-Py-700 exhibited the highest specific capacitance at 1 A g^{-1} of 317 F g^{-1} closely followed by N-Ben-800 of 283 F g^{-1} (Table S2).

CV studies of P-N-HCP-Δ materials at a scan rate of 10 mV s^{-1} are shown in Fig. 2g. P-N-Ben-600 shows relatively low current response, yielding a capacitance of 51 F g^{-1}. This is attributed to the low levels of N-doping (1.40%) at 600 °C and the decrease in surface area from 538 m^2 g^{-1} for C-Ben-800–425 m^2 g^{-1}. Nevertheless, the post NH_3 carbonization increased its supercapacitive behavior from its precursor, which had a capacitance of 33 F g^{-1} at the same scan rate. Using a higher post-synthesis NH_3 carbonization temperature of 800 °C resulted in a higher surface area (697 m^2 g^{-1}) and N-content (5.17%) in P-N-Ben-800, which yields a higher specific capacity of 158 F g^{-1}. P-N-Py-600 displayed a capacitance of 135 F g^{-1}, close to its precursor of 126 F g^{-1}, even with a higher surface area and N-content. Interestingly, P-N-Py-700 yields a higher capacitance of 162 F g^{-1} despite its surface area being close to that of P-N-Py-600 and having a lower N-content (8.51% for P-N-Py-700 *vs.* 11.52% for P-N-Py-600). This is thought to be due to the better conductivity of P-N-Py-700 as higher post-carbonization temperatures are used, as evidenced by a more vertical low frequency region of P-N-Py-700 in the Nyquist plot which is shifted away from the real axis along lower resistive values (Fig. S7) [63]. P-N-Py-700 exhibits a slightly higher capacitance than P-N-Ben-800, likely due to the higher N-content and therefore PC contribution from P-N-Py-700. However, as P-N-Ben-800 has a larger surface area, thus EDLC contribution, it retains more capacitance at higher scan rates than P-N-Py-700 (Fig. 2h). GCD of P-N-HCP-Δ materials at a current density of 1 A g^{-1} show that they retain a triangular charge-discharge shape (Fig. 2i). Though high capacitances of up to 231 F g^{-1} were obtained for P-N-Py-700 at a current density of 1 A g^{-1}, the N-Ben-800 and N-Py-700 displayed superior supercapacitive behavior compared to the post NH_3 carbonized materials.

N-Ben-800 and N-Py-700 showed excellent supercapacitive behavior; N-Ben-800 has a higher surface area and a good N-content, whereas N-Py-700 has a lower surface area but higher N-content. The CV results of N-Ben-800 at scan rates between 10 and 200 mV s^{-1} are shown in Fig. 3a. The CV retains a highly symmetric quasi-rectangular shape when the scan rate was increased, with the capacitance only reducing from 267 F g^{-1} at 10 mV s^{-1} to 205 F g^{-1} at 200 mV s^{-1}, demonstrating excellent capacitance retention of 77%. Moreover, a specific capacitance of 171 F g^{-1} was observed at an extremely high scan rate of 1000 mV s^{-1}. Voltammetric currents of the material also swiftly reach their respective plateau when the direction of the potential sweep is changed; even with scan rates as fast as 1000 mV s^{-1} (Fig. 3b). N-Ben-800 possesses a low equivalent series resistance (ESR) which is due to its high electric conductivity and low ionic resistance of the electrolyte in the pores during charging and discharging [65]. GCD curves between 0.1 and 10 A g^{-1} retains a consistent symmetrical triangular shape with the varying current densities (Fig. 3c&d), exhibiting excellent capacitances of 295 F g^{-1} at 0.1 A g^{-1}, 283 F g^{-1} at 1 A g^{-1} and 239 F g^{-1} at 10 A g^{-1}, a capacitance retention of 81% between 0.1 and 10 A g^{-1}. The Nyquist plot of N-Ben-800 in the low frequency region shows the impedance of the imaginary part approaches vertical, demonstrating ideal capacitive behavior (Fig. 3e). The capacitances of N-Ben-800 can be calculated from the imaginary part of the impedance spectrum which shows increasing capacitance with lower applied frequencies (Fig. 3f). The capacitance behavior is visible at frequencies below 10 Hz [66], with the curve in the low frequency range (10–0.01 Hz) approaching almost horizontal to ~300 F g^{-1}. Interestingly, though capacitance increases with lower applied frequencies for N-Py-700, the curve does not plateau at the lower frequency range. This is thought to be due to the slower kinetics of N-Py-700, which is more pseudocapacitive than N-Ben-800, and therefore may require even lower applied frequencies to begin plateauing (*i.e.,* full utilization of PC).

N-Py-700 is highly symmetrical between scan rates of 10 and 200 mV s^{-1} (Fig. 3g) which confirms its good electrochemical stability and capacitance [24,67,68], with high specific capacitances of 284 F g^{-1} at 10 mV s^{-1} and 164 F g^{-1} at 200 mV s^{-1}, a capacitance

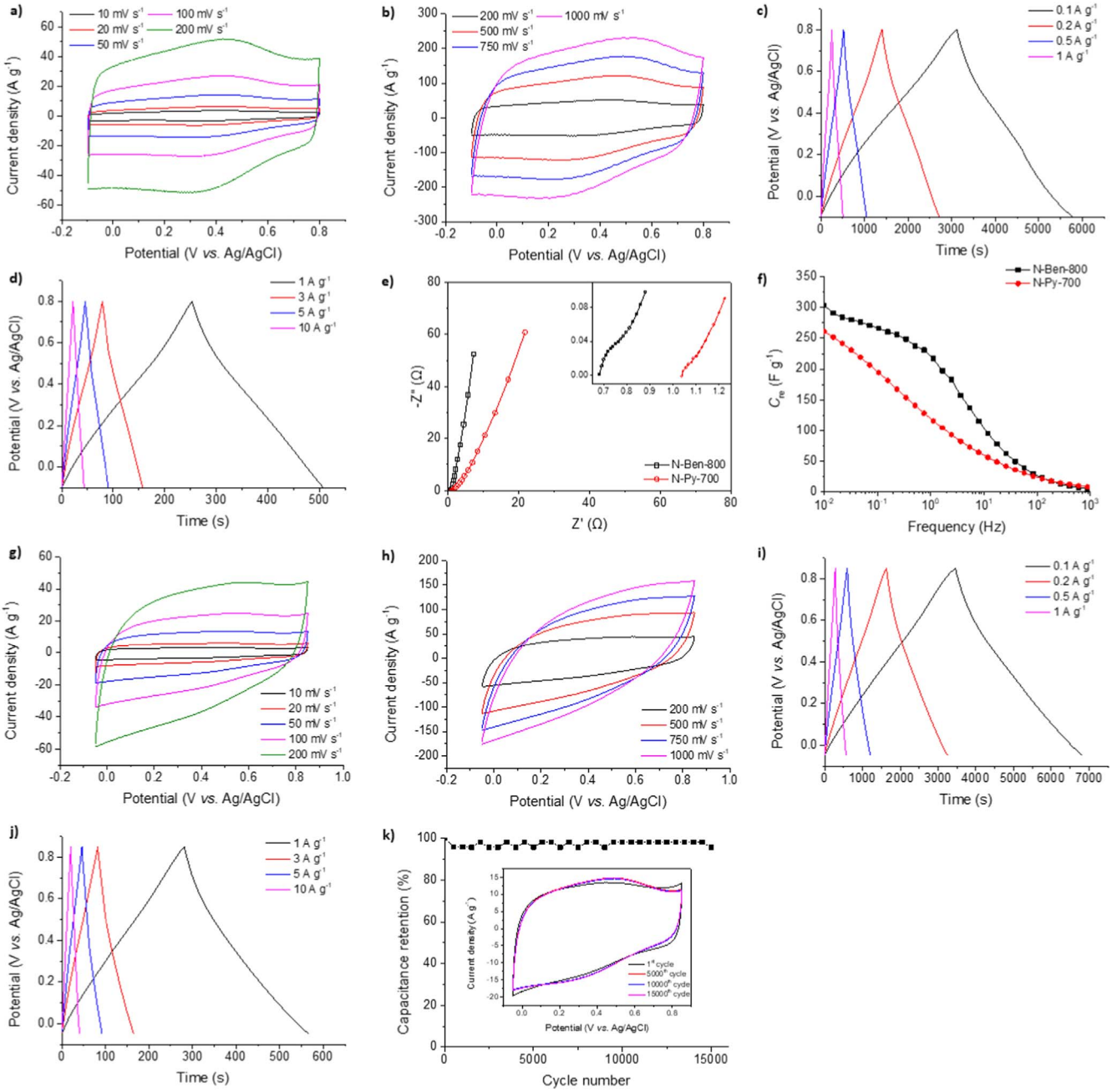

Fig. 3. Electrochemical analysis of the optimized carbonized materials in a three-electrode system in 1 M H_2SO_4. (a) Cyclic voltammograms of N-Ben-800 at varying scan rates between 10 and 200 mV s^{-1}. (b) Cyclic voltammograms of N-Ben-800 at varying scan rates between 200 and 1000 mV s^{-1}. (c) Galvanostatic charge-discharge curves of N-Ben-800 at current densities between 0.1 and 1 A g^{-1}. (d) Galvanostatic charge-discharge curves of N-Ben-800 at current densities between 1 and 10 A g^{-1}. (e) Nyquist impedance spectrum of N-Ben-800 and N-Py-700 measured at 400 mV *vs.* Ag/AgCl. Inset shows the results in the high frequency region. (f) Frequency dependence of specific capacitance for N-Ben-800 and N-Py-700 at 400 mV *vs.* Ag/AgCl. (g) Cyclic voltammograms of N-Py-700 at varying scan rates between 10 and 200 mV s^{-1}. (h) Cyclic voltammograms of N-Py-700 at varying scan rates between 200 and 1000 mV s^{-1}. (i) Galvanostatic charge-discharge curves of N-Py-700 at current densities between 0.1 and 1 A g^{-1}. (j) Galvanostatic charge-discharge curves of N-Py-700 at current densities between 1 and 10 A g^{-1}. (k) Cycling stability test of N-Py-700 at a current density of 5 A g^{-1}. Inset shows the CV of N-Py-700 at a scan rate of 50 mV s^{-1} after the 1st, 5000th, 10,000th, and 15,000th cycle.

retention of 58%. The capacitance retention is lower than N-Ben-800 because N-Ben-800 has a larger surface area, and hence the capacitance is mainly attributed to the EDLC mechanism, which has fast electrochemical kinetics [7]. By contrast, N-Py-700 has a relatively low surface area but higher N-content, hence its capacitance is mainly attributed to the PC mechanism, which is known to give lower power densities [9]. This is more evident at very high scan rates (*e.g.*, 1000 mV s^{-1}) which yields a capacitance of 82 F g^{-1}. Although the capacitance at 1000 mV s^{-1} is relatively low, its CV shape retains high symmetry and possesses a more quasi-rectangular profile than other expensive and optimized materials (Fig. 3h) [22,30,47], even when they are run at lower scan rates. GCD experiments of N-Py-700 between current densities of 0.1 and 10 A g^{-1} all display symmetrical triangular profiles (Fig. 3i&j), indicating the material has typical supercapacitor behavior. Exceptionally, the material exhibits an extremely high capacitance of 374 F g^{-1} at 0.1 A g^{-1}. This is higher than some of the best performing organic materials (Table 2) such as N-doped carbons [69–71], B/N-co-doped porous carbon (BNC-9) [72], N-doped carbon nanotubes (PNCNTs) [73], N-doped graphene [74], N-doped microspheres (A-PNCM) [75], and more costly networks such as covalent triazine

Table 2
Specific capacitances of a selection of top performing organic materials reported in the literature.

Sample	Capacitance ($F g^{-1}$)	Current density ($A g^{-1}$)	Potential window (V)	Electrolyte	References
N-Py-700	374	0.1	0.9	1 M H_2SO_4	This work
Porous N-doped carbon (CA-GA-2)	300	0.1	1.0	1 M H_2SO_4	[69]
N-doped carbon from PANI	235	1.0	1.0	1 M H_2SO_4	[70]
N-doped mesoporous carbon (H-NMC-2.5)	262	0.2	0.9	1 M H_2SO_4	[71]
B/N-co-doped porous carbon (BNC-9)	268	0.1	1.0	6 M KOH	[72]
Porous N-doped carbon nanotubes (PNCNTs)	210	0.5	1.0	6 M KOH	[73]
N-doped graphene	282	< 1	0.8	6 M KOH	[74]
Porous N-doped carbon microspheres (A-PNCM)	282	0.5	1.0	6 M KOH	[75]
2-D Covalent triazine framework	151	0.1	3.0	$EMIMBF_4$	[77]
Terephthalonitrile-derived N-rich network (TNNs-550)	298	0.2	1.0	1 M H_2SO_4	[76]
N-doped carbon from CMP (N3-CMP-1)	260	0.1	1.1	3 M KOH	[10]
Carbon from pyrene-based CMP (SDBPy-800)	301	1.0	0.9	6 M KOH	[23]
Triazatruxene-based CMP (TAT-CMP-2)	183	1.0	1.0	1 M Na_2SO_4	[78]
Carbon from PAF (K-PAF-1)	280	1.0	0.8	6 M KOH	[22]
Carbon from MOF (MAC-A)	274	0.25	1.0	6 M KOH	[27]
Core-shell nanoporous carbon from MOF and PANI (carbon-PANI core-shell)	236	1.0	0.8	1 M H_2SO_4	[29]

framework- [76,77], CMP- [10,23,78], PAF- [22], and MOF-derived carbonaceous materials [27,29]. N-Py-700 also outperforms carbons with surface areas > 3000 $m^2 g^{-1}$ [79], exemplifying the importance of heteroatom doping in porous carbons to produce high performing supercapacitive materials. Moreover, N-Py-700 shows excellent stability, with 95.8% capacitance retention after 15,000 charge-discharge cycles at a current density of 5 $A g^{-1}$ (Fig. 3k). The CV shape shifts to a more quasi-rectangular shape from the 1st to 5000th cycle, presumably due to the initial activation period that allows progressive wetting of the pores during cycling (Fig. 3k, inset). The 5000th, 10,000th, and 15,000th CV cycle shows very little change, indicating minimum degradation of N-Py-700 after cycling. Both N-Ben-800 and N-Py-700 were also tested at extremely high current densities of up to 100 $A g^{-1}$ (Fig. S8) and showed capacitances of 162 and 88 $F g^{-1}$, respectively (Fig. S9). This represents a 68% and 39% capacitance retention for N-Ben-800 and N-Py-700, respectively, upon increasing the current density from 10 to 100 $A g^{-1}$. N-Ben-800 performs better at faster rates due to its higher proportion of EDLC. Ragone plots show that the N-Ben-800 and N-Py-700 exhibit maximum energy and power densities of 42 $W h kg^{-1}$ and 4.5 $kW kg^{-1}$, respectively (Fig. S10). The energy densities of the optimized materials reaches the regime of batteries such as Pb-acid, NiCd, and Li-ion (10–150 $W h kg^{-1}$), whilst being over one order of magnitude in power density than those of batteries (< 0.3 $kW kg^{-1}$) [8].

Full cell supercapacitors of N-Ben-800 and N-Py-700 were constructed in order to study the materials in a practical device and to minimize any errors which may cause overestimation of capacitance in the three-electrode method [80]. A symmetrical two-electrode set-up was used containing the charge balanced material in 1 M H_2SO_4 and showed results consistent with the three-electrode method (Fig. 4). The CV shape of N-Ben-800 is highly quasi-rectangular at scan rates between 10 and 200 $mV s^{-1}$ (Fig. 4a)—even more so than during the three-electrode method (Fig. 3a)—and retains this shape at scan rates up to 1000 $mV s^{-1}$ (Fig. 4b). The current response in the two-electrode configuration is slightly larger at 0 V as the open-circuit potential of N-Ben-800 in the three-electrode configuration was found to be 0.4 V—the middle of the redox couple in N-Ben-800. The capacitance was found to be 229 $F g^{-1}$ at 10 $mV s^{-1}$ and 163 $F g^{-1}$ at the very high scan rate of 1000 $mV s^{-1}$ (Fig. 4c). The GCD curves of N-Ben-800 are symmetric and linear, with negligible voltage drop demonstrating low internal resistance and ideal capacitive behavior in the full cell set-up with a high capacitance of 211 $F g^{-1}$ at 1 $A g^{-1}$ (Fig. 4d). The Nyquist plot in the two-electrode set-up similarly shows phase angles close to 90° demonstrating ideal capacitive behavior, with a slight deviation at very low frequencies due to the pseudocapacitive contributions of N-Ben-800 readily occurring at these low frequencies (Fig. 4e). The capacitance from impedance spectroscopy is almost horizontal at the low frequency range (10 to 0.01 Hz), reaching a stable capacitance of 230 $F g^{-1}$. The CV shape of N-Py-700 between 10 and 1000 $mV s^{-1}$ are all quasi-rectangular (Fig. 4g&h), indicating ideal capacitive performance, more so than during the three-electrode configuration (Fig. 3g&h), thus these materials are suitable for practical devices. Interestingly, the capacitance of N-Py-700 in the two-electrode configuration at 10 $mV s^{-1}$ was similar to N-Ben-800 (222 *vs.* 229 $F g^{-1}$) but the capacitance retention was lower at higher scan rates due to its pseudocapacitive nature (Fig. 4c). The GCD curves of N-Py-700 in the two-electrode configuration also retained its symmetric triangular shape, demonstrating its ideality as a supercapacitor material, with a capacitance of 199 $F g^{-1}$ at 1 $A g^{-1}$ (Fig. 4i). The Nyquist plot of N-Py-700 approaches vertical with a phase angle of 83°—higher than in the three-electrode configuration—showing ideal capacitive behavior (Fig. 4e). Additionally, the Bode plot of the two-electrode configuration also shows a plateau towards 83° at lower frequencies compared against the three-electrode configuration, supporting the material as an ideal capacitor for practical applications (Fig. S11).

3.4. Differentiating between EDLC and PC mechanisms

In order to better understand the supercapacitive contributions from the surface area and from the heteroatom-doping, it is valuable to quantify the relative contributions from EDLC and PC. The respective EDLC and PC contributions from the heteroatom-doped carbons can be compared against each other due to the relatively slower electrochemical kinetics from Faradaic redox reactions of N- and S-containing functional groups in the PC mechanism compared to the faster EDLC process [48]. The maximum total specific capacitance, $C_{S,T,M}$, can be partitioned into EDLC contributions, C_{DL}, and PC contributions, C_P, by using the same procedure developed to estimate the outer electroactive sites of metal oxides [81–83]. In this partition procedure, the total voltammetric charge, q_T, is calculated by extrapolation of voltammetric charge to $v = 0$ from the plot of $1/q$ *vs.* $v^{1/2}$ (Fig. 5a). Charge associated with the double-layer, q_{DL}, is calculated by the extrapolation of voltammetric charge to $v = \infty$ from the plot of q *vs.* $v^{-1/2}$ (Fig. 5b). Therefore, charge associated with PC, q_P, can be obtained by the difference between q_T and q_{DL}. Thus, specific capacitance from the maximum total ($C_{S,T,M}$), EDLC (C_{DL}), and PC (C_P), contributions can be calculated by dividing the corresponding charge with their respective potential windows used in CV (Table 3).

All of the heteroatom-doped carbons possess both EDLC and PC contributions. As expected, higher overall PC contributions, $C_P/C_{S,T,M}$, are obtained where there are high levels of heteroatoms combined with relatively low surface areas, the latter of which decreases the EDLC

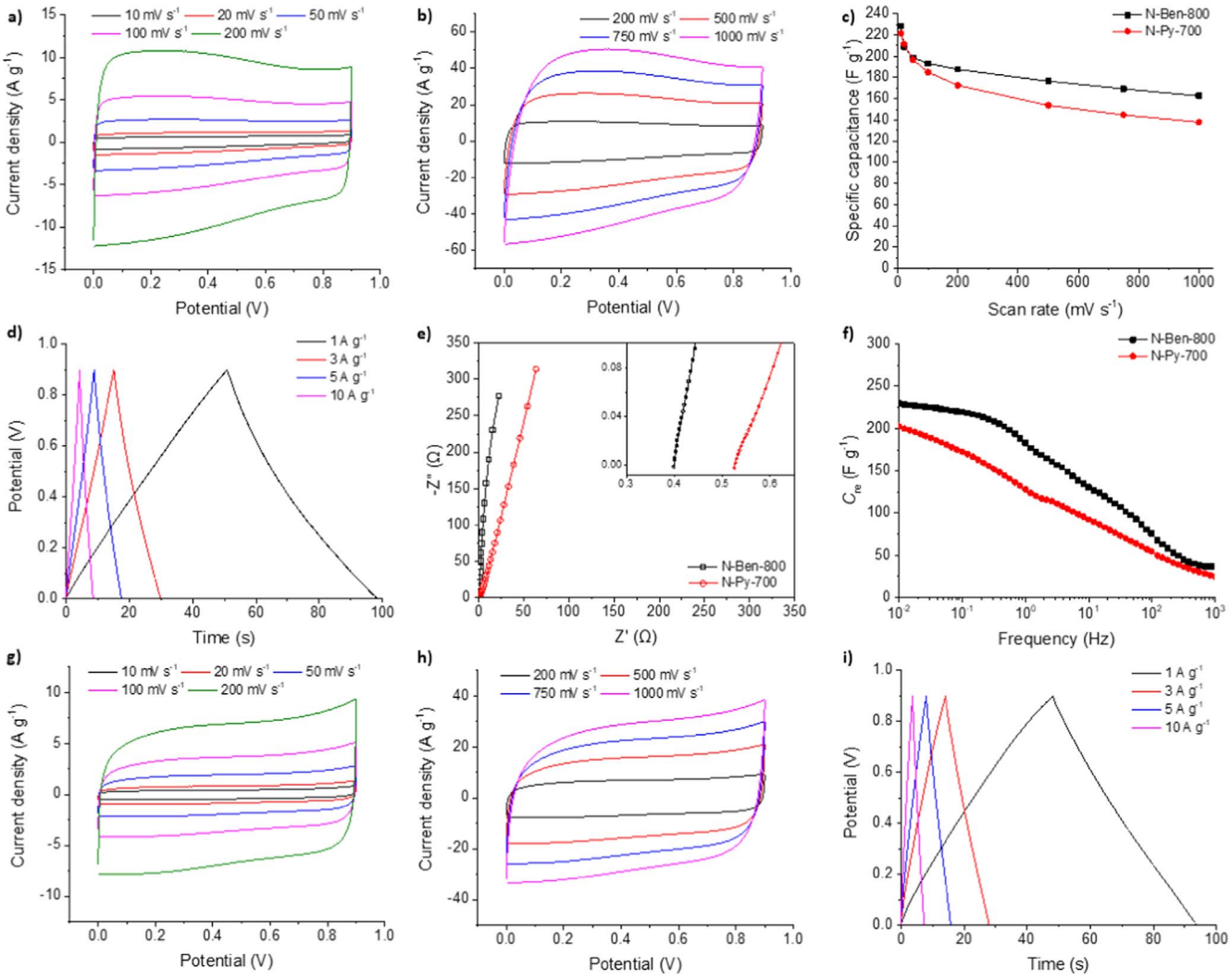

Fig. 4. Electrochemical analysis of the optimized carbonized materials in a two-electrode system in 1 M H_2SO_4. (a) Cyclic voltammograms of N-Ben-800 at varying scan rates between 10 and 200 mV s^{-1}. (b) Cyclic voltammograms of N-Ben-800 at varying scan rates between 200 and 1000 mV s^{-1}. (c) Specific capacitance of N-Ben-800 and N-Py-700 at varying scan rates. (d) Galvanostatic charge-discharge curves of N-Ben-800 at current densities between 1 and 10 A g^{-1}. (e) Nyquist impedance spectrum of N-Ben-800 and N-Py-700 measured at 0 V. Inset shows the results in the high frequency region. (f) Frequency dependence of specific capacitance for N-Ben-800 and N-Py-700 at 0 V. (g) Cyclic voltammograms of N-Py-700 at varying scan rates between 10 and 200 mV s^{-1}. (h) Cyclic voltammograms of N-Py-700 at varying scan rates between 200 and 1000 mV s^{-1}. (i) Galvanostatic charge-discharge curves of N-Py-700 at current densities between 1 and 10 A g^{-1}.

contribution. The low temperature carbonizations materials prepared at 600 °C (N-Ben-600, N-Py-600, and N-Th-600) generally have very high $C_P/C_{S,T,M}$ as low electric conductivity result in lower EDLC contributions. N-Ben-700 has a slightly higher surface area and lower N-content than N-Ben-600, resulting in a lower $C_P/C_{S,T,M}$ (43.2% *vs*. 80.4%). N-Ben-800, which is the best supercapacitive material in its series, has the highest C_{DL} of 197 F g^{-1} attributed to its high surface area of 1252 m^2 g^{-1}, and it results in a $C_P/C_{S,T,M}$ of 25.5%; it is therefore a strongly EDLC-biased material. Even though the N-content of N-Ben-1000 is lower than N-Ben-800, the $C_P/C_{S,T,M}$ is higher due to the reduction of surface area in the material, and thus the C_{DL} contribution. The $C_P/C_{S,T,M}$ of P-N-Ben-600 and P-N-Ben-800 is very similar (38.1% and 38.2%, respectively), as the increase in surface area and N-content in P-N-Ben-800 increases both C_{DL} and C_P. As expected, N-Py-700 has the highest $C_{S,T,M}$ of 444 F g^{-1}, which is in line with yielding the highest capacitance of all materials at a scan rate of 10 mV s^{-1}. This is largely attributed to the high C_P of 279 F g^{-1} from its high N-content of 13.44%, resulting in a $C_P/C_{S,T,M}$ of 62.9%. N-Py-800, which has a higher surface area than N-Ben-800, has a lower C_{DL}, in line with the pore structure of N-Ben-800 facilitating better electrolyte ion diffusion kinetics and, hence, EDLC. However, the N-content and C_P of N-Py-800 is higher than N-Ben-800, leading to a larger $C_P/C_{S,T,M}$ of 35.7%. C-Th-800 has a relatively low $C_P/C_{S,T,M}$ of 53.6%, despite possessing a high S-content of 13.58% (*c.f.* C-Py-700: N-content = 9.42%, $C_P/C_{S,T,M}$ = 69.4%; N-Py-700: N-content = 13.44%, $C_P/C_{S,T,M}$ = 62.9%), which may be due to S-groups providing lower PC contributions than N-groups, as discussed above. This is further supported by comparing N-Th-600 with N-Th-800, which have similar N-contents but the C_P of N-Th-800 (60 F g^{-1}) is higher than N-Th-600 (35 F g^{-1}), despite containing no S-atoms; this is likely due to increased electric conductivity from the higher carbonization temperatures. Surprisingly, although N-Th-700 has a high N-content, it has a low $C_P/C_{S,T,M}$ of 14.6% compared with others in its series, and thus a high EDLC contribution. This could be due to N-groups in N-Th-700 increasing electrical conductivity [21] and increased dipolar attraction to the electrolyte cations [47] in the relatively high surface area carbon, aiding the EDLC mechanism. X-ray photoelectron spectroscopy (XPS) was also measured for various samples to check the O-content of the materials (Table S3). The carbonizations integrated a similar amount of O species into the materials (8.16–10.83%) so it was assumed that O-content does not greatly affect this study due to the consistent levels across samples. The XPS and CHNS values of C and N vary slightly due to differences of the surface

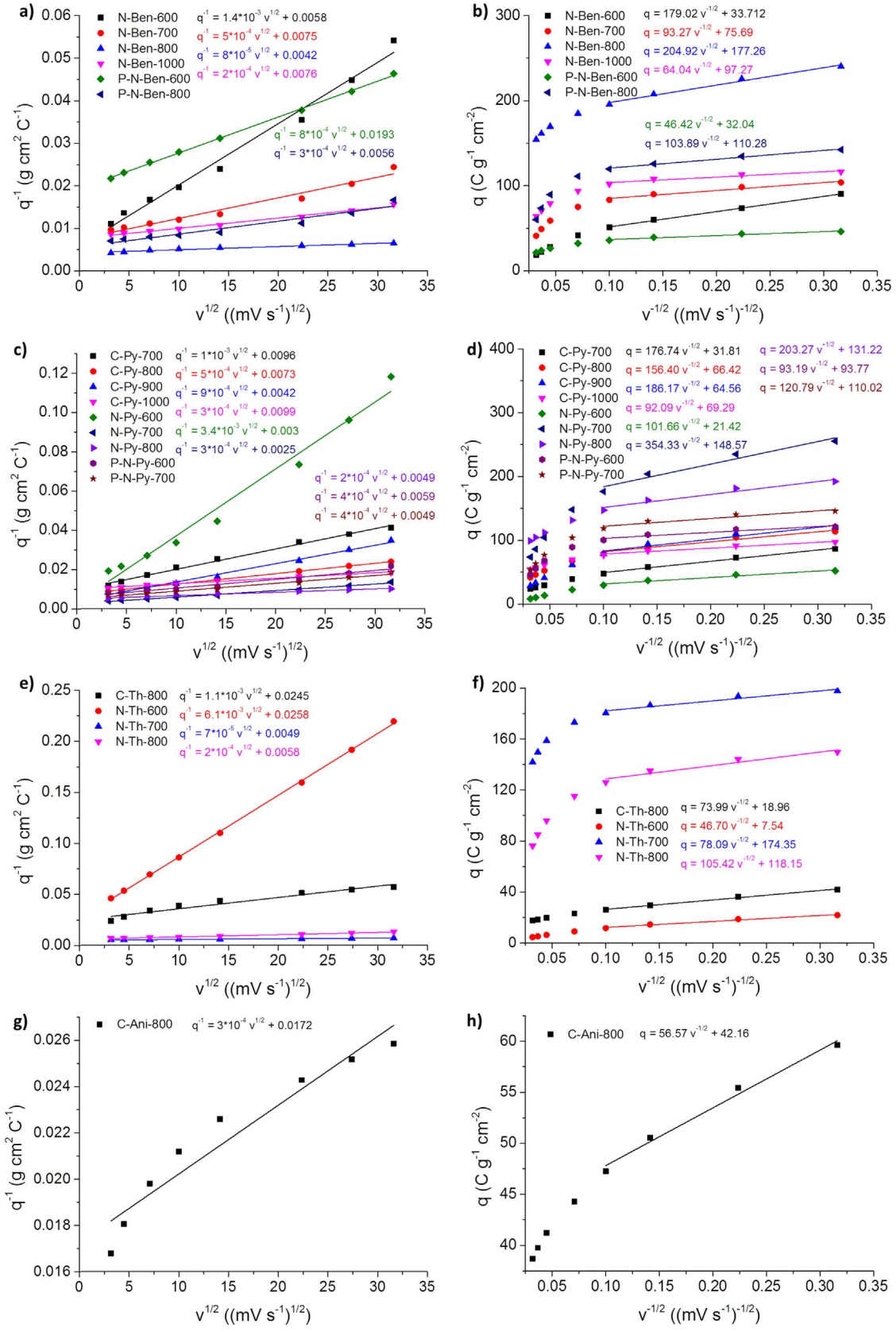

Fig. 5. (a, c, e, g) Dependence of $1/q$ *vs.* $v^{1/2}$ and (b, d, f, h) dependence of q *vs.* $v^{-1/2}$ for heteroatom doped HCP-based carbons in 1 M H_2SO_4.

Table 3
Summary of maximum total specific capacitance ($C_{S,T,M}$), double-layer capacitance ($C_{S,DL}$), and pseudocapacitance ($C_{S,P}$) of heteroatom doped HCP-based carbons in 1 M H_2SO_4.

Sample	$C_{S,T,M}$ (F g^{-1})	C_{DL} (F g^{-1})	C_P(F g^{-1})	$C_P/C_{S,T,M}$ (%)
N-Ben-600	192	37	154	80.4
N-Ben-700	148	84	64	43.2
N-Ben-800	264	197	67	25.5
N-Ben-1000	147	108	39	26.3
P-N-Ben-600	58	36	22	38.1
P-N-Ben-800	198	123	76	38.2
C-Py-700	116	35	80	69.4
C-Py-800	152	76	78	51.5
C-Py-900	265	72	193	72.8
C-Py-1000	112	77	65	31.4
N-Py-600	370	24	347	93.6
N-Py-700	444	165	279	62.9
N-Py − 800	194	125	69	35.7
P-N-Py-600	188	104	84	44.7
P-N-Py-700	227	111	116	50.1
C-Th-800	51	24	27	53.6
N-Th-600	43	8	35	80.5
N-Th − 700	227	194	33	14.6
N-Th-800	192	131	60	31.4
C-Ani-800	65	47	18	27.5

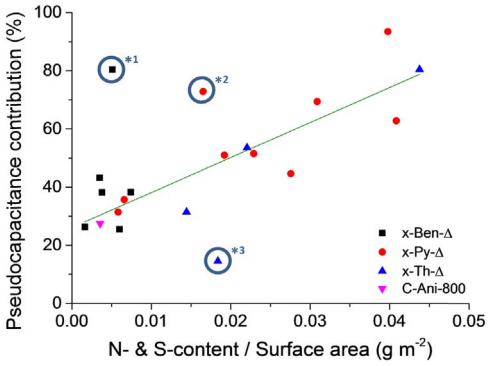

Fig. 6. Correlation of overall pseudocapacitance contributions against N- & S-content to surface area ratio. *1 = N-Ben-600. *2 = N-Py-600. *3 = N-Th-700. Heteroatom-content is taken from CHNS.

and overall composition, however the N-content of XPS follows the same trend as CHNS.

This partition capacitance model has generally been used for either comparing very similar materials [48,82,83], or for comparing a single material in different electrolytes [10,81], where perhaps 2 or 3 samples are compared. Hence, factors that may affect the partitioning, such as electric conductivity, pore structure, wettability, and morphology, are assumed to be the same. Due to the large sample size of this study (20 samples), there are some small deviations against the line of best fit shown in Fig. 5a,c,g. The $C_P/C_{S,T,M}$ contributions of these materials can also be plotted against the normalised heteroatom to surface area ratio (Fig. 6). In general we found that $C_P/C_{S,T,M}$ in the HCP-based carbons is, approximately, linearly proportional to the ratio of heteroatom-doping to surface area, irrespective of the carbonization precursor. The three outliers in the plot are a result of low electric conductivity in N-Ben-600 and N-Py-600, and the high EDLC contributions in N-Th-700, as discussed above. N-Th-600 could also be considered as an outlier due to its low electric conductivity if S-doping is not accounted for (Fig. S12). A combination of EDLC and PC contributions is important for supercapacitive materials, with their ratio yielding different electrochemical storage behavior, as exhibited by the two best-performing carbons, N-Ben-800 and N-Py-700, which have a $C_P/C_{S,T,M}$ of 25.5% and 62.9%, respectively.

Though it is widely known that redox-active, heteroatom-doped carbons contribute to PC [7,10,48,60–62], this study uncovers the direct quantitative contribution that heteroatom-doping provides. To our knowledge, this is the first time that such a large range of materials has been studied and their EDLC and PC contributions compared.

4. Conclusions

In summary, we have shown that the carbonization of HCPs through various methods can be used to generate carbons with excellent supercapacitive properties. Our method produces conductive carbons using low-cost precursors, while allowing heteroatoms to be incorporated by choice of feedstock and by changing the type of gas used in the carbonization. A 63% PC-based material, N-Py-700, shows ideal supercapacitive behavior, with a very high capacitance of 374 F g^{-1} at 0.1 A g^{-1}, and retains 96% capacitance after 15,000 charge-discharge cycles. N-Ben-800, which shows 74% EDLC, exhibits a capacitance of 295 F g^{-1} at 0.1 A g^{-1} with an excellent capacitance retention of 81% at a very high current density of 10 A g^{-1}. The EDLC and PC contributions of the HCP-based carbons were quantified and compared against their properties, allowing synthetic control over the two supercapacitive mechanisms. There is a near endless synthetic diversity to form HCPs by this route, since more than 25 million aromatic molecules are susceptible to the Friedel-Crafts alkylation [39]. Hence, it is likely that further supercapacitive HCP-based carbons will be produced that exhibit improved energy storage properties over the promising materials presented here.

Acknowledgements

The authors thank the EPSRC (EP/N004884/1) for financial support. Sheng-Chi Lin and Jeng-An Wang are thanked for two-electrode set-up advice. X-ray photoelectron spectra were obtained at the National EPSRC XPS Users' Service (NEXUS) at Newcastle University, an EPSRC Mid-Range Facility. J.-S. M. L thanks ESPRC (EP/L505018/1) for a DTA studentship.

Appendix A. Supporting information

Supplementary data associated with this article can be found in the online version at http://dx.doi.org/10.1016/j.nanoen.2018.01.042.

References

[1] J.W. Choi, D. Aurbach, Nat. Rev. Mater. 1 (2016) 16013.
[2] J.M. Tarascon, M. Armand, Nature 414 (2001) 359–367.
[3] H. Vikström, S. Davidsson, M. Höök, Appl. Energy 110 (2013) 252–266.
[4] J.R. Miller, P. Simon, Science 321 (2008) 651.
[5] Y. Zhu, S. Murali, M.D. Stoller, K.J. Ganesh, W. Cai, P.J. Ferreira, A. Pirkle, R.M. Wallace, K.A. Cychosz, M. Thommes, D. Su, E.A. Stach, R.S. Ruoff, Science 332 (2011) 1537.
[6] A. Burke, J. Power Sources 91 (2000) 37–50.
[7] P. Simon, Y. Gogotsi, Nat. Mater. 7 (2008) 845–854.
[8] R. Kötz, M. Carlen, Electrochim. Acta 45 (2000) 2483–2498.
[9] B. You, L. Wang, L. Yao, J. Yang, Chem. Commun. 49 (2013) 5016–5018.
[10] J.-S.M. Lee, T.-H. Wu, B.M. Alston, M.E. Briggs, T. Hasell, C.-C. Hu, A.I. Cooper, J. Mater. Chem. A 4 (2016) 7665–7673.
[11] W. Fan, Y.-Y. Xia, W.W. Tjiu, P.K. Pallathadka, C. He, T. Liu, J. Power Sources 243 (2013) 973–981.
[12] D.-W. Wang, F. Li, L.-C. Yin, X. Lu, Z.-G. Chen, I.R. Gentle, G.Q. Lu, H.-M. Cheng, Chem. - Eur. J. 18 (2012) 5345–5351.
[13] L. Wang, G. Mu, C. Tian, L. Sun, W. Zhou, P. Yu, J. Yin, H. Fu, ChemSusChem 6 (2013) 880–889.
[14] E. Raymundo-Piñero, F. Leroux, F. Béguin, Adv. Mater. 18 (2006) 1877–1882.
[15] J. Deng, M. Li, Y. Wang, Green Chem. 18 (2016) 4824–4854.
[16] T. Zhu, J. Zhou, Z. Li, S. Li, W. Si, S. Zhuo, J. Mater. Chem. A 2 (2014) 12545–12551.
[17] L. Wei, M. Sevilla, A.B. Fuertes, R. Mokaya, G. Yushin, Adv. Funct. Mater. 22 (2012) 827–834.
[18] Y. Li, X. Xu, Y. He, Y. Jiang, K. Lin, Polymers 9 (2017) 2.
[19] L. Zhang, F. Zhang, X. Yang, G. Long, Y. Wu, T. Zhang, K. Leng, Y. Huang, Y. Ma, A. Yu, Y. Chen, Sci. Rep. 3 (2013) 1408.
[20] M. Xue, D. Chen, X. Wang, J. Chen, G.F. Chen, J. Mater. Chem. A 3 (2015)

7715–7718.
[21] Y. Qiu, X. Zhang, S. Yang, Phys. Chem. Chem. Phys. 13 (2011) 12554–12558.
[22] Y. Li, S. Roy, T. Ben, S. Xu, S. Qiu, Phys. Chem. Chem. Phys. 16 (2014) 12909–12917.
[23] Y. Zhao, F. Xie, C. Zhang, R. Kong, S. Feng, J.-X. Jiang, Microporous Mesoporous Mater. 240 (2017) 73–79.
[24] J.P. Zheng, P.J. Cygan, T.R. Jow, J. Electrochem. Soc. 142 (1995) 2699–2703.
[25] W. Sugimoto, Ruthenium Oxides as Supercapacitor Electrodes, in: G. Kreysa, K.-I. Ota, R.F. Savinell (Eds.), Encyclopedia of Applied Electrochemistry, Springer New York, New York, NY, 2014, pp. 1813–1821.
[26] A. Funke, F. Ziegler, Bioresour. Technol. 102 (2011) 7595–7598.
[27] J. Hu, H. Wang, Q. Gao, H. Guo, Carbon 48 (2010) 3599–3606.
[28] R.R. Salunkhe, Y.V. Kaneti, J. Kim, J.H. Kim, Y. Yamauchi, Acc. Chem. Res. 49 (2016) 2796–2806.
[29] R.R. Salunkhe, J. Tang, N. Kobayashi, J. Kim, Y. Ide, S. Tominaka, J.H. Kim, Y. Yamauchi, Chem. Sci. 7 (2016) 5704–5713.
[30] Z. Xiang, D. Wang, Y. Xue, L. Dai, J.-F. Chen, D. Cao, Sci. Rep. 5 (2015) 8307.
[31] K. Yuan, P. Guo-Wang, T. Hu, L. Shi, R. Zeng, M. Forster, T. Pichler, Y. Chen, U. Scherf, Chem. Mater. 27 (2015) 7403–7411.
[32] H. Wang, Z. Cheng, Y. Liao, J. Li, J. Weber, A. Thomas, C.F.J. Faul, Chem. Mater. 29 (2017) 4885–4893.
[33] L. Tan, B. Tan, Chem. Soc. Rev. 46 (2017) 3322–3356.
[34] V.A. Davankov, M.P. Tsyurupa, React. Polym. 13 (1990) 27–42.
[35] W. Li, A. Zhang, H. Gao, M. Chen, A. Liu, H. Bai, L. Li, Chem. Commun. 52 (2016) 2780–2783.
[36] M.P. Tsyurupa, L.A. Maslova, A.I. Andreeva, T.A. Mrachkovskaya, V.A. Davankov, React. Polym. 25 (1995) 69–78.
[37] B. Li, R. Gong, W. Wang, X. Huang, W. Zhang, H. Li, C. Hu, B. Tan, Macromolecules 44 (2011) 2410–2414.
[38] R. Dawson, E. Stockel, J.R. Holst, D.J. Adams, A.I. Cooper, Energy Environ. Sci. 4 (2011) 4239–4245.
[39] J.-S.M. Lee, M.E. Briggs, T. Hasell, A.I. Cooper, Adv. Mater. 28 (2016) 9804–9810.
[40] S. Wang, C. Zhang, Y. Shu, S. Jiang, Q. Xia, L. Chen, S. Jin, I. Hussain, A.I. Cooper, B. Tan, Sci. Adv. 3 (2017).
[41] T. Mitra, R.S. Bhavsar, D.J. Adams, P.M. Budd, A.I. Cooper, Chem. Commun. 52 (2016) 5581–5584.
[42] C.H. Lau, X. Mulet, K. Konstas, C.M. Doherty, M.-A. Sani, F. Separovic, M.R. Hill, C.D. Wood, Angew. Chem. Int. Ed. 55 (2016) 1998–2001.
[43] Z.-A. Qiao, S.-H. Chai, K. Nelson, Z. Bi, J. Chen, S.M. Mahurin, X. Zhu, S. Dai, Nat. Commun. 5 (2014) 3705.
[44] R. Dawson, A.I. Cooper, D.J. Adams, Prog. Polym. Sci. 37 (2012) 530–563.
[45] S. Xu, Y. Luo, B. Tan, Macromol. Rapid Commun. 34 (2013) 471–484.
[46] Z. Dou, L. Xu, Y. Zhi, Y. Zhang, H. Xia, Y. Mu, X. Liu, Chem. - Eur. J. 22 (2016) 9919–9922.
[47] Y. Kou, Y. Xu, Z. Guo, D. Jiang, Angew. Chem. Int. Ed. 50 (2011) 8753–8757.
[48] Y.-H. Lee, K.-H. Chang, C.-C. Hu, J. Power Sources 227 (2013) 300–308.
[49] M. Thommes, K. Kaneko, A.V. Neimark, J.P. Olivier, F. Rodriguez-Reinoso, J. Rouquerol, K.S.W. Sing, Pure Appl. Chem. 87 (2015) 1051–1069.
[50] V. Davankov, M. Tsyurupa, Chapter 7 - Properties of Hypercrosslinked Polystyrene, in: A.D. Vadim, P.T. Maria (Eds.), Comprehensive Analytical Chemistry, Elsevier, 2011, pp. 195–295.
[51] R. Dawson, T. Ratvijitvech, M. Corker, A. Laybourn, Y.Z. Khimyak, A.I. Cooper, D.J. Adams, Polym. Chem. 3 (2012) 2034–2038.
[52] Z. Song-lin, G. Shang-yu, Y. Xi-gen, X. Bo-sen, J. For. Res. 14 (2003) 75–79.
[53] L. Qie, W.-M. Chen, Z.-H. Wang, Q.-G. Shao, X. Li, L.-X. Yuan, X.-L. Hu, W.-X. Zhang, Y.-H. Huang, Adv. Mater. 24 (2012) 2047–2050.
[54] S. Gao, H. Fan, Y. Chen, L. Li, Y. Bando, D. Golberg, Nano Energy 2 (2013) 1261–1270.
[55] C. Hu, Y. Xiao, Y. Zhao, N. Chen, Z. Zhang, M. Cao, L. Qu, Nanoscale 5 (2013) 2726–2733.
[56] N.J. Bell, Y.H. Ng, A. Du, H. Coster, S.C. Smith, R. Amal, J. Phys. Chem. C 115 (2011) 6004–6009.
[57] M. Inagaki, K. Feiyu, Carbon Materials Science and Engineering: From Fundamentals to Applications (清华大学出版社有限公司), Tsinghua University Press, 2006.
[58] Z. Dai, C. Peng, J.H. Chae, K.C. Ng, G.Z. Chen, Sci. Rep. 5 (2015) 9854.
[59] E. Raymundo-Piñero, M. Cadek, F. Béguin, Adv. Funct. Mater. 19 (2009) 1032–1039.
[60] X. Chen, R. Paul, L. Dai, Natl. Sci. Rev. 4 (2017) 453–489.
[61] A. Borenstein, O. Hanna, R. Attias, S. Luski, T. Brousse, D. Aurbach, J. Mater. Chem. A 5 (2017) 12653–12672.
[62] M. Sevilla, R. Mokaya, Energy Environ. Sci. 7 (2014) 1250–1280.
[63] P.L. Taberna, P. Simon, J.F. Fauvarque, J. Electrochem. Soc. 150 (2003) A292–A300.
[64] K. Xia, Q. Gao, J. Jiang, J. Hu, Carbon 46 (2008) 1718–1726.
[65] F.-C. Wu, R.-L. Tseng, C.-C. Hu, C.-C. Wang, J. Power Sources 159 (2006) 1532–1542.
[66] T.-H. Wu, C.-T. Hsu, C.-C. Hu, L.J. Hardwick, J. Power Sources 242 (2013) 289–298.
[67] C. Largeot, C. Portet, J. Chmiola, P.-L. Taberna, Y. Gogotsi, P. Simon, J. Am. Chem. Soc. 130 (2008) 2730–2731.
[68] X. Feng, Y. Liang, L. Zhi, A. Thomas, D. Wu, I. Lieberwirth, U. Kolb, K. Müllen, Adv. Funct. Mater. 19 (2009) 2125–2129.
[69] L. Zhao, L.-Z. Fan, M.-Q. Zhou, H. Guan, S. Qiao, M. Antonietti, M.-M. Titirici, Adv. Mater. 22 (2010) 5202–5206.
[70] L. Li, E. Liu, J. Li, Y. Yang, H. Shen, Z. Huang, X. Xiang, W. Li, J. Power Sources 195 (2010) 1516–1521.
[71] J. Wei, D. Zhou, Z. Sun, Y. Deng, Y. Xia, D. Zhao, Adv. Funct. Mater. 23 (2013) 2322–2328.
[72] H. Guo, Q. Gao, J. Power Sources 186 (2009) 551–556.
[73] G. Xu, B. Ding, P. Nie, L. Shen, J. Wang, X. Zhang, Chem. - Eur. J. 19 (2013) 12306–12312.
[74] H.M. Jeong, J.W. Lee, W.H. Shin, Y.J. Choi, H.J. Shin, J.K. Kang, J.W. Choi, Nano Lett. 11 (2011) 2472–2477.
[75] J. Han, G. Xu, H. Dou, D.R. MacFarlane, Chem. - Eur. J. 21 (2015) 2310–2314.
[76] L. Hao, B. Luo, X. Li, M. Jin, Y. Fang, Z. Tang, Y. Jia, M. Liang, A. Thomas, J. Yang, L. Zhi, Energy Environ. Sci. 5 (2012) 9747–9751.
[77] L. Hao, J. Ning, B. Luo, B. Wang, Y. Zhang, Z. Tang, J. Yang, A. Thomas, L. Zhi, J. Am. Chem. Soc. 137 (2015) 219–225.
[78] X.-C. Li, Y. Zhang, C.-Y. Wang, Y. Wan, W.-Y. Lai, H. Pang, W. Huang, Chem. Sci. 8 (2017) 2959–2965.
[79] E. Raymundo-Piñero, K. Kierzek, J. Machnikowski, F. Béguin, Carbon 44 (2006) 2498–2507.
[80] M.D. Stoller, R.S. Ruoff, Energy Environ. Sci. 3 (2010) 1294–1301.
[81] S. Ardizzone, G. Fregonara, S. Trasatti, Electrochim. Acta 35 (1990) 263–267.
[82] D. Baronetto, N. Krstajić, S. Trasatti, Electrochim. Acta 39 (1994) 2359–2362.
[83] K.-H. Chang, C.-C. Hu, C.-Y. Chou, Chem. Mater. 19 (2007) 2112–2119.

Jet-Sing M. Lee received his MChem degree (2013) at the University of Liverpool, UK, which included a research year in industry at Ineos. He is currently a PhD candidate at the same university under the supervision of Prof. Andrew I. Cooper. During his PhD, he received a Global Engineering Leadership scholarship to undergo a placement abroad in Taiwan with Prof. Chi-Chang Hu. His research interests include porous materials, carbonizations, energy storage, and environmental applications. He is currently at Kyoto University as a Japan Society for the Promotion of Science (JSPS) fellow.

Michael Briggs is a Research Coordinator in the group of Prof. Andrew Cooper at the University of Liverpool. After Graduating from the University of Hull (1998), he undertook a PhD at the University of Leeds (2002), before undertaking postdoctoral research at the École polytechnique in Paris (2004). This was followed by a number of years in industry carrying out custom synthesis, development, and scale up projects, before joining the University of Liverpool (2010). Michael's research interests include the development of new synthetic methods for the production of porous organic materials for gas capture, separations, energy storage, and catalysis.

Chi-Chang Hu received his bachelor's degree in 1991 and Ph.D. in chemical engineering from National Cheng Kung University in 1995. After receiving his Ph.D., he joined National Chung Cheng University as an assistant professor (1997), associate professor (2000), and full professor (2003). He joined National Tsing Hua University in 2007 and is presently working as university chair professor at the Department of Chemical Engineering, National Tsing Hua University, Taiwan. He has published more than 240 SCI publications with a total number of citations more than 11,000 and H-index = 55.

Andy Cooper is Professor of Chemistry at the University of Liverpool, UK. He is the founding Director of the Centre for Materials Discovery, established in 2007, and was Head of Chemistry and then the first Head of the School of Physical Sciences in the period 2007–2012. He led the UK RPIF bid to establish the Materials Innovation Factory, which opened in 2017, and is its first Academic Director. He is also the Director of the Leverhulme Centre for Functional Materials Design. Andy's research interests are polymeric materials, porous materials, supramolecular chemistry, and materials for energy production and storage.